

**Monte Carlo simulations of dusty spiral galaxies:  
extinction and polarization properties**

Simone Bianchi

Univ. di Firenze Dipartimento di Astronomia e Scienza dello Spazio

Largo E. Fermi, 5, 50125 Firenze, Italy

Andrea Ferrara and Carlo Giovanardi

Osservatorio Astrofisico di Arcetri

Largo E. Fermi, 5, 50125 Firenze, Italy

Received \_\_\_\_\_; accepted \_\_\_\_\_

## ABSTRACT

We present Monte Carlo simulations of dusty spiral galaxies, modelled as bulge + disk systems, aimed to study their extinction and polarization properties. The extinction parameters (absorption and scattering) of dust grains are calculated from Mie’s theory for a full distribution of sizes and materials; the radiation transfer is carried on for the four Stokes parameters. Photometric and polarimetric maps of galaxies of different optical depths, inclinations and bulge-to-total ratios have been produced in the B and I bandpasses. As expected, the effect of scattering is to reduce substantially the extinction for a given optical depth, in particular for what concerns the obscuration of bright bulge cores. For the same reason, scattering reduces also the reddening, as evaluated from B-I maps. On the other hand the bluing directly due to forward scattering is hardly appreciable. Radial color gradients are often found. A comparison with “sandwich” models shows that they fail dramatically to reproduce the extinction - optical depth relation. The degree of linear polarization produced by scattering is usually of the order of a few percent; it increases with optical depth, and with inclination ( $i \leq 80^\circ$ ). The polarization pattern is always perpendicular to the major axis, unless the dust distribution is drastically modified. There is little local correlation between extinction and polarization degree and there is a trend of increasing polarization from the B to the I band. We discuss implications and relevance of the results for studies of the structure and morphology of spiral galaxies and of their interstellar medium.

*Subject headings:* dust,extinction—galaxies: spiral—methods: numerical—polarization—radiative transfer—scattering

## 1. Introduction

For a long time, since Holmberg’s first analysis (Holmberg 1958), disk galaxies, including the gas-rich late morphological types, have been taken as largely transparent systems. Although with various refinements, this point of view has been shared by the authors of catalogs of galaxies, such as the relatively recent Revised Shapley-Ames Catalog of Bright Galaxies (Sandage & Tamman 1981), and thereby adopted by the majority of the astronomical community. Holmberg inferred average values of the internal extinction on statistical grounds, that is by interpreting the correlation between inclination and mean surface brightness in a rather limited sample of 119 spirals of various morphologies. On the other hand, refined studies of the dust content and distribution of individual, representative galaxies are scarce. In the edge-on Sc galaxy NGC 891, Kylafis & Bahcall (1987) have been able to determine an overall transparency of the disk, when seen face-on, in a bandpass around 6000Å.

Recently, however, some studies have shaken the widespread belief in transparent disks (Disney, Davies & Phillipps 1989; Valentijn 1990) and the issue has rapidly become one of the most contended in the literature on normal galaxies, sometimes with opposite conclusions drawn by the analysis of the same, or similar, set of data (Valentijn 1994). The idea of opaque galaxies has gained in the last years a certain acceptance and has been shared by the recent Third Reference Catalogue of Bright Galaxies (de Vaucouleurs et al. 1991).

This debate on the optical thickness of galactic disks is relevant to a number of issues important for extragalactic astronomy. We mention: (i) the morphology and internal structure of galactic components, such as bulges, disks, lenses, bars, etc; (ii) the dark matter content of galaxies and clusters, and (iii) the luminosity corrections affecting redshift-independent measures of distances. The last point, in particular, touches on the

field of the large scale structure of the universe, and of the deviations from the Hubble flow.

For these reasons, observations and data analyses are becoming more refined with particular reference to selection biases (Burstein, Haynes & Faber 1991), to redshift information (Chołoniewski 1991; Giovanelli et al. 1994) and to multiwavelength imaging (Peletier et al. 1994; Evans 1994). At the same time the modelling has also become increasingly sophisticated. In fact, as it has been argued by most of the already cited authors, a fundamental problem in statistical evaluations of the extinction lies in the absence of accurate and sensitive observable indicators. Surface brightness, diameters and colors have often been interpreted in the framework of models so naive and unrealistic to yield too simplistic and sometimes wrong results.

A realistic modelling of dusty disks is thus strongly required. Besides, if we postulate the possibility of large optical thicknesses and sizeable grain albedos, as it is the case for wavelengths shorter than  $3\mu\text{m}$ , then the effect of multiple scattering in composite (bulge + disk) systems, with dust interspersed with stars, must be included (e.g. Block et al. 1994). A remarkable progress on this track is achieved in the recent paper by Byun, Freeman & Kylafis (1994, hereafter BFK) who have produced simulations of disk galaxies of various morphology and optical thickness. Their treatment of the radiative transfer includes exactly the contribution of the first scattering, and approximately the higher scattering orders. They adopt a Henyey-Greenstein phase function and a single dust grain with average optical properties according to Draine & Lee (1984).

Scattering events are also expected to introduce polarization in the otherwise unpolarized emission from normal stars. Polarimetric studies of normal spirals, both observational and theoretical ones, are scarce. In view of the current interest in the properties of dusty disks such scarcity is remarkable since most of the information about the physical properties of dust grains is locked into their polarization effects. Among the few

observations of this kind, we mention the detailed studies of M31, M82, M104, and of the Magellanic clouds; they are summarized and referenced by Wielebinski & Krause (1993).

One of the fields where the analysis and simulation of polarization maps has been most effective in recent years is star formation, and, in particular, the study of protostellar envelopes (see Fischer, Henning & Yorke, 1994 and references therein). Here the more recent and detailed models are based on Monte Carlo simulations which allow for arbitrary distributions of polydisperse mixtures of spherical dust particles. In all these models any observed polarization is imputed to transfer effects on light which is otherwise emitted unpolarized by stars. In particular, since dust grains are usually assumed to be spherical, homogeneous and optically isotropic, only the polarizing effect of scattering is taken into account. It is widely known, anyway, that in our Galaxy the linear polarization introduced by the light propagation through the interstellar medium is best described as the effect of dichroic absorption by aligned, elongated grains (Spitzer 1978; Gledhill & Scarrot 1989). Sometimes, this polarization mechanism has been questioned but, indeed, only for particular situations, where the presence of a suitable toroidal magnetic field, that is the main ingredient for the alignment, is dubious or improbable (Menard 1989).

We present here the results of Monte Carlo simulations of realistic model galaxies within the frame of Mie's scattering theory, that is for spherical dust grains with homogeneous and isotropic optical properties. In our study the dust grain is not a single, average one but instead we allow for a mixture of different materials and a continuous distribution of size. The phase function is consistently computed from Mie's theory for each grain. The radiation transfer is exact to any scattering order and complete for the four Stokes parameters, so that the output can be analyzed in the form of polarimetric, as well as photometric, maps. Stars and dust three-dimensional distributions are the ones commonly accepted, and similar to those adopted by BFK. The present paper deals only with scattering events on spherical

grains and does not include any dichroism in the absorption itself. The polarization properties may, therefore, be different from those produced by needles rotating, as widely believed, in a galactic meridian plane.

Although we deal in this study with the simplest of the realistic cases, that is, smooth distributions and spherical grains, the Monte Carlo method is ideal to probe more hostile situations. The effect of clumping in the obscuring dust, of non-spherical dust grains and of extinction by gas at short wavelengths are deferred to future papers.

## 2. A dusty galaxy model

In the following we describe the model distribution here adopted to simulate the spatial distribution of the photon emitters (stars) and of the particles contributing to extinction (dust).

### 2.1. Stellar distributions

We describe the stellar spatial distribution in a spiral galaxy by two components: a spheroidal bulge and a 3-dimensional disk. We neglect dark massive halos, since we are only interested in luminous components, and also possible small-scale inhomogeneities such as spiral arms and star-forming regions.

#### 2.1.1. Bulge

The surface brightness profiles of spheroidal systems is usually well described by the  $R^{1/4}$  law (de Vaucouleurs 1959):

$$I(R) = I_e 10^{-3.33[(R/R_e)^{1/4}-1]}, \quad (1)$$

where  $R_e$  is the equivalent radius, and  $I_e$  is the surface brightness of the corresponding isophote; both  $R$  and  $R_e$  are measured on the sky plane. For numerical purpose, it is convenient to have an analytical expression for the bulge luminosity density  $\rho^{(b)}$ , which can be obtained deprojecting the profiles. Since there is no simple, analytical expression for  $\rho^{(b)}$  corresponding to equation (1) (see Young 1976) we choose to adopt the Jaffe distribution which corresponds to the luminosity density (Jaffe 1983):

$$\rho^{(b)}(\tilde{r}) = \frac{\rho_0^{(b)}}{(\tilde{r}/r_b)^2 [1 + (\tilde{r}/r_b)]^2}, \quad (2)$$

where  $\tilde{r}$  is the physical distance from the galactic center, and  $r_b$  is the scale radius for which we adopt  $r_b = 1.16 R_e$  (see Appendix A.1.1).

In principle, there is no need for an external truncation radius for the Jaffe distribution since the volume integral converges for  $\tilde{r} \rightarrow \infty$ ; for numerical purposes, though, we have introduced a truncation radius  $r_{max}^{(b)} = nr_b$ . In fact, in absence of an external truncation, at large radii the bulge's light will dominate once again that of the (exponential) disk. In the simulations presented here, we have adopted the values  $R_e = 1.60$  kpc,  $n = 8$ . The value for  $R_e$  is close to the one inferred for our Galaxy; the value for  $n$  is such that  $r_{max}^{(b)}$  corresponds to the point where the ratio between the bulge luminosity density and the density of the adopted disk is maximum (Sect. 2.1.2).

### 2.1.2. Disk

The assumed luminosity density distribution for the disk is (Freeman 1970)

$$\rho^{(d)}(r, z) = \rho_0^{(d)} \exp(-r/r_d) Z(z/z_d), \quad (3)$$

where  $r$  and  $z$  are the cylindrical radius and the height above the equatorial plane of the galaxy, respectively, and the constants  $r_d$ ,  $z_d$  are the relative scale lengths; The function

$Z(z/z_d)$  describes the vertical behavior of the distribution, which is assumed to be either exponential or of the type "sech<sup>2</sup>" (van der Kruit & Searle 1981; Wainscoat, Freeman & Hyland 1989); the results presented in this paper are for the exponential vertical distribution that is

$$Z(z/z_d) = \exp(-|z|/z_d). \quad (4)$$

In analogy with the bulge case, we have introduced a horizontal,  $r_{max}^{(d)} = mr_d$ , and a vertical  $z_{max}^{(d)} = kz_d$  external truncation. Our models are for  $r_d = 4.0$  kpc,  $z_d = 0.35$  kpc, which are similar to what is observed for the old disk population of the Galaxy; for the external truncations we adopt  $m = k = 6$ .

### 2.1.3. *bulge/total luminosity ratios*

To simulate different Hubble types, we have run models with different bulge/total luminosity ratios ranging from 0 (resembling an Sd galaxy, BT00) to 0.5 (Sa, BT05). All our simulations are monochromatic and we have run models at the effective wavelengths of the B and I bandpasses, 4400 and 9000Å respectively. Possible differences in the stellar population of the two components are taken into account by adopting a B-I color of the bulge larger than that of the disk. More precisely the luminosity of the bulge has been increased by one magnitude in the I band while the luminosity of the disk has been kept constant in both bands; therefore we suppose an intrinsic B-I=0 for the disk and B-I=1 for the bulge.

All of these prescriptions conform to those adopted by BFK.



## 2.2. Dust properties

The only absorbing particles included in our code are dust grains; we neglect the absorption above the Lyman limit due to diffuse hydrogen gas, the possible presence of molecules, etc. .

### 2.2.1. Dust disk

The dust is supposed to be smoothly <sup>1</sup> distributed in a disk with the same law (eq. [3]) as for the stellar disk

$$\rho^{(g)}(r, z) = \rho_0^{(g)} \exp(-r/r_g)Z(z/z_g). \quad (5)$$

where  $r_g$  and  $z_g$  are the horizontal and vertical dust scale lengths. In this paper we are mainly interested in determining the effects of a *standard* dust layer on the structural parameters and appearance of a galaxy, we will devote a following paper to study the detailed structure and distribution of dust as inferred from the observed light distribution in spiral galaxies. The Galactic parameters for the dust distribution are by far more uncertain than for the stars. For the computations presented here, we have assumed  $r_g = 4.0$  kpc,  $z_g = 0.14$  kpc and the same truncation factor as for the stellar disk. That is, while the radial extents of the stellar and dust disk are identical, we will always deal with dust disks which are vertically embedded into the star distribution. This is an important point, since several of the results in the following will be determined by the presence of sizeable stellar emission outside the obscuring layer.

We assume that the dust physical properties (i.e. the grain size distribution and materials, see below) are independent of the position in the galaxy and therefore the

---

<sup>1</sup>A study of the effects introduced by dust clumping is in progress.

absorption coefficient at wavelength  $\lambda$  can be written as  $k_\lambda = \langle C^{ext}(\lambda) \rangle \rho^{(g)}(r, z)$ , where  $\langle C^{ext}(\lambda) \rangle$  is the extinction cross section per unit mass, averaged over the grain distribution and materials (see eq. [7]).

It is common to normalize the total content of dust in the galaxy in terms of the optical depth along the symmetry axis of the galaxy,

$$\tau_\lambda(0) = \int_{-\infty}^{\infty} \sigma_\lambda \rho^{(g)}(r=0, z) dz = 2 \langle C^{ext}(\lambda) \rangle \rho_0^{(g)} z_g, \quad (6)$$

both for the exponential and  $\text{sech}^2$  distributions. As for the stellar disk, the results here presented refer to vertically exponential dust disks.

### 2.2.2. Dust components and size distribution

In our model the grains are supposed to be spherical and to have a size distribution given by the MRN model (Mathis, Rumpl & Nordsiek 1977),  $n(a) \propto a^{-3.5}$ , where  $a$  is the grain radius. We consider three materials: astronomical silicates,  $\parallel$  graphite, and  $\perp$  graphite. The numerical silicates/graphite ratio is 1:1.12, with 1/3 of the graphite having optical properties measured parallel ( $\parallel$ ), and 2/3 perpendicular ( $\perp$ ) to the c-axis. The lower and upper limits of the distribution are  $a_- = 0.005 \mu\text{m}$  and  $a_+ = 0.25 \mu\text{m}$ , irrespectively of the material. Very small grains and PAH have not been included due to the large uncertainties both in their size distribution and optical constants.

The dielectric constants adopted are the ones given by Draine & Lee (1984), recently extended in the far UV and X-rays by Martin & Rouleau (1991). All the relevant optical properties (absorption and scattering cross section, albedo, phase function, and Mueller matrix) have been calculated using Mie formulae. The resulting extinction curve is illustrated in Fig. 1.

EDITOR: PLACE FIGURE 1 HERE.

In our models the central optical depth of the disk is defined by  $\tau_V(0)$  the value at 5500Å; models at different wavelengths are still defined by  $\tau_V(0)$  but all computations of optical thickness are scaled according to our extinction curve.

### 2.2.3. Comparison with Henyey-Greenstein approximation

The average value of a quantity  $q$ , over the dust distribution, is here defined as

$$\langle q \rangle = \frac{\sum_i w_i \int_{a_-}^{a_+} q C_i^{ext} n_i(a) da}{\sum_i w_i \int_{a_-}^{a_+} C_i^{ext} n_i(a) da}, \quad (7)$$

where  $C_i^{ext}$  is the extinction cross section, the index  $i$  refers to the material, and  $w_i$  is its weight in the distribution; both  $q$  and  $C_i^{ext}$  depend on  $\lambda$

Previous works dealing with scattering problems have often approximated the phase function  $\Phi$  with the Henyey-Greenstein (HG) formula (Henyey & Greenstein 1941),

$$\Phi(\theta, \phi) = \frac{1}{4\pi} \frac{1 - g^2}{(1 + g^2 - 2g \cos \theta)^{3/2}}, \quad (8)$$

where  $g$  is the asymmetry parameter (that is the average value of  $\cos \theta$  weighted by the phase function);  $\theta$  and  $\phi$  are the polar and azimuthal scattering angles, respectively.

In Fig. 2 we show a comparison between the average phase function for the distribution calculated with the Monte Carlo procedure implemented in our radiative transfer code and the HG phase function for which a value of  $g$  averaged on the distribution according to equation (7) has been used. The differences between the two phase functions are striking (as an example, the B and I bands are shown): *the HG approximation always underestimates the forward scattering* by as much as 25 %, the difference being larger in the B band.

EDITOR: PLACE FIGURE 2 HERE.

For the albedo and asymmetry parameter we obtain  $\langle \tilde{\omega} \rangle = 0.53$  and  $\langle g \rangle = 0.38$  in the B-band, and  $\langle \tilde{\omega} \rangle = 0.50$  and  $\langle g \rangle = 0.21$  in the I-band.

### 3. Monte Carlo simulation

Monte Carlo methods allow the life of each photon to be followed through scattering and absorption processes. Here we provide a brief description of our computational scheme, deferring the interested reader to the Appendix for a more detailed presentation.

#### 3.1. Emission cycle

We determine first the position of the photon emission point, according to the bulge and disk luminosities as described in Sect. 2.1. Photons are emitted isotropically and unpolarized. The Stokes parameters are defined for each photon on the plane perpendicular to its propagation vector, following the conventions in Shurcliff (1962); the reference direction on such plane is the projection of the galactic  $z$  axis (i.e. the symmetry axis). All photons are emitted with the same intensity, or strength, that is with the first Stokes parameter  $I = 1$ . The emission cycle requires five random numbers: three for the position and two for the direction (see Appendix A.1).

#### 3.2. Scattering cycle

Then we determine the position of the scattering point, i.e., the position at which the photon collides with a dust grain; grains are assumed to be distributed as described in Sect. 2.2. This implies to determine first an optical depth  $\tau$  for the scattering point, and then the

geometrical position along the line of propagation where this  $\tau$  is actually reached. It turns out that this second step is the most consuming, in terms of computational time, of the whole process (Appendix A.2). Once the position of the scattering event is known, we pass to determine the characteristics of the dust grain, according to the size and composition distributions (Appendix A.3). Note that in principle such a sequence renders rather straightforward to allow for situations where the physical properties of dust vary within the galaxy, e.g. with galactocentric distance. These steps require two more random numbers, one to locate the diffusion point, the other to fix the size and composition of the scatterer. Knowing the radius and refractive index of the grain (together with  $\lambda$ ), it is now possible to compute the (polar) phase function and the albedo, and, by extracting a new random number, to choose the (polar) angle of scattering  $\theta$ . Together with the geometro-optical properties of the dust grain, and within the frame of Mie’s theory,  $\theta$  determines completely the elements of the scattering (Mueller) matrix. The matrix elements also enter into the expression for the azimuthal phase function, so that, by extracting a new, final random number we define completely direction and Stokes vector of the scattered photon (see Appendix A4).

The updated Stokes parameters are calculated via the following transformation

$$\begin{pmatrix} I' \\ Q' \\ U' \\ V' \end{pmatrix} \propto \mathbf{R}'\mathbf{M}\mathbf{R} \begin{pmatrix} I \\ Q \\ U \\ V \end{pmatrix}. \quad (9)$$

The rotation matrix  $\mathbf{R}$  transforms the initial Stokes parameters into a new set whose reference direction for linear polarization lies in the scattering plane.  $\mathbf{M}$  is the relevant Mueller matrix with reference to the scattering plane, which depends only on  $\theta$  and on the dust properties; the matrix  $\mathbf{R}'$  provides the final transformation of the Stokes parameters to the final reference direction, that is the projection of the  $z$  axis onto the plane normal

to the new direction of propagation. In our formulation we make use of normalized Mueller matrices, the absolute values of the Stokes parameter are adjusted according to the incoming intensity  $I$  and to the albedo of the scatterer. In summary a single scattering cycle needs the extraction of four random numbers: one to locate the diffusion point, one to choose the size and type of grain, and two for the direction of the scattered photon. The scattering cycle is iterated until the photon escapes the dust layer. or dies because its strength  $I$  goes below a threshold value ( $I_{lim} = 10^{-4}$ ).

### 3.3. Output and performance

The output of the code consists of  $N_B$  maps, for each Stokes parameter, where  $N_B$  is the number of bands of different galaxy inclination to the line of sight (Appendix A.5). The models presented here are obtained with  $N_B = 15$ , and each map has an extent of 201x201 pixels, with a spatial resolution of 0.2 kpc; the resolution is therefore moderate both in space and in inclination.

A full model (bulge+disk) with enough signal to noise ratio to distinguish a clear polarization pattern in the outer parts of the galaxy (with linear polarization degree of  $\sim 1\%$ ) required a number of photon launches of the order of  $10^8$ . Anyway, photometric accuracies comparable to those of astronomical images are usually attainable with less than  $10^7$  launches. The code has been tested on a variety of more simple and predictable situations: point sources within spherical scattering envelopes, Rayleigh scattering, optically thin regimes, absorption only, etc..

## 4. Results

In summary, the models presented here were all obtained for: bulge effective radius  $R_e = 1.6$  kpc, truncated at 15 kpc; disk radial scale length  $r_d = 4.0$  kpc, truncated at 24 kpc; disk exponential vertical scale length  $z_d = 0.35$  kpc, truncated at 2.1 kpc; dust radial scale length  $r_g = 4.0$  kpc, truncated at 24 kpc; dust exponential vertical scale length  $z_g = 0.14$  kpc, truncated at 0.84 kpc. All of the results obtained do not depend on the adopted truncation factor as far as they exceed 5 scale lengths.

We ran simulations for 6 different values of  $\tau_V(0)$ : 0.0, 0.5, 1.0, 2.0, 5.0, 10.0; and for 4 different B/T ratios: 0.0, 0.1, 0.3, 0.5. The average angle <sup>2</sup> to the line of sight of the 8 independent inclination bands, was  $\langle\theta\rangle = 20^\circ, 37^\circ, 48^\circ, 58^\circ, 66^\circ, 75^\circ, 82^\circ, 90^\circ$ .

All these models were produced both at 4400Å for the B-band, and at 9000Å, for the I-band. We also ran some simulations, although not a complete set, at 3500Å (U-band).

### 4.1. Extinction properties

Since the adopted range of parameters conforms to the one used by BFK, we can directly compare our results with theirs. All the results about minor and major axis profiles<sup>3</sup>, total extinction, face-on corrections, isophote shapes and diameters agree

---

<sup>2</sup>As defined by  $\langle\theta\rangle_i = \int_{\theta_i^-}^{\theta_i^+} \theta \sin\theta d\theta$ , where  $\theta_i^-$  and  $\theta_i^+$  are the limiting values for the  $i$ -th inclination band.

<sup>3</sup>The shape of the major axis profiles of systems with conspicuous bulges, inclinations  $<80^\circ$  and  $\tau_V(0)>2$ , resemble closely the Type II profiles defined by Freeman (1970). Anyway, as noted by the same author, they often show up also in galaxies with a low dust content, such as S0's, and therefore their explanation seems to require peculiar stellar distributions

remarkably well and therefore we refer to their work (for a more thorough discussion see Bianchi 1995). Most of differences between our results and those of BFK are mainly imputable to the choice of the extinction law. While BFK use the empirical data of Rieke & Lebofsky (1985), that gives  $A_B = 1.32A_V$ , we conform to the MRN and Draine & Lee (1984) model (Sect. 2.2.2, Fig. 1) and obtain  $A_B = 1.28A_V$ . Additional differences arise from the finite spatial resolution of our images and from the finite resolution in inclination to the line of sight, as explained in appendix A.5. However these differences are relevant only when intensity varies greatly with position and inclination (the edge-on case)

We point out that the central surface brightness of disks with large optical depth still varies with inclination due to stars not immersed in dust, if indeed the dust scale height is smaller than for stars. In addition, in the B-band, the difference between edge-on and face-on central surface brightness is the same for models with  $\tau_V(0) \geq 2$ , corresponding to 0.3 magnitudes. This common behavior makes the study of central surface brightness unsuitable to the determination of the optical depth of the dust disk in spiral galaxies. As for the influence of scattering, the main (and obvious) result is a substantial reduction of the actual extinction for a given  $\tau_V(0)$ . As illustrated in Fig. 3, such reduction is higher for greater  $\tau_V(0)$  and lower inclination, with a maximum of  $\sim 0.3$  mag for B-band models. For edge-on models, the difference is less than 0.1 mag, so that neglecting the effect of scattering when fitting the brightness profiles of highly inclined objects can be rather justified (Ohta & Kodaira 1995).

EDITOR: PLACE FIGURE 3 HERE.

---

in addition to extinction effects.



#### 4.1.1. Local extinction

The differences between models including scattering and models with absorption only can also be appreciated by analyzing the local extinction. In Fig. 4 we plot the central extinction ( $r = 0$ ) for models in the B band ( $A_B$ ) with  $i = 20^\circ$  (our inclination nearest to face-on) as a function of the central optical depth  $\tau_V(0)$ .

EDITOR: PLACE FIGURE 4 HERE.

The straight line corresponds to the Holmberg screen model, while dotted ones to sandwich models (Disney *et al.* 1989) with different  $\xi$ , the dust-to-stellar thickness ratio. The left panel is for models with absorption only, while the right panel includes the scattering: screen and sandwiches are the same in both panels, and only include absorption.

Models with absorption only show that the behavior of the central extinction in the pure disk models (BT00) can be described locally by a sandwich with  $\xi = 0.6$ , while models including a bulge require inverse sandwiches, that is with dust extending higher than stars from the equatorial plane ( $\xi = 1.1$ ). This is because the bulk of the emission at the center, that is the bulge core, is located inside the dust layer.

In models with scattering (right panel) we note that the central extinction is reduced by several tenths of magnitude since the radiation has a good probability to be diffused by the dust, rather than absorbed. This is because, with our assumptions about the dust composition and size distribution, the average albedo amounts to  $\sim 0.5$ , both in the B and I-band. Moreover the behavior of scattering models is very different from that of sandwiches.

In Fig. 5 we show the extinction at  $r = r_d$  on the major axis, as a function of the local vertical optical depth, for the same models as in Figure 4. Since the bulge contribution

is small at this distance, all the models present nearly the same behavior, principally regulated by the disk. Also, models with scattering show again that sandwiches are a poor approximation. It is interesting to note that for  $\tau_V(0) < 0.5$  scattering plays such a role that extinction is basically absent.

EDITOR: PLACE FIGURE 5 HERE.

#### *4.1.2. Images and color maps*

Intensity images and B-I color maps bring additional information. In Fig. 6 we show images in the B-band and color maps for a bulge, a disk and a BT05 model, with inclination  $82^\circ$  and  $\tau_V(0)=10$ . Since the extinction for bulge and disk is due to the same dust disk, the BT05 model is simply a superposition of the first two images. We have used the same gray scale for the intensity images, while color maps have different scales to evidence the details.

EDITOR: PLACE FIGURE 6 HERE.

Extinction is more pronounced in the bulge because stars and dust are not homogeneously mixed and the dust acts almost like a screen. However, extinction also modifies the shape of the disk which becomes asymmetric with respect to the major axis. Color maps are positive everywhere, also in pure disks (intrinsic B-I=0), indicating a general reddening. The red color of the outer "halo" in the BT05 maps is due to the intrinsic (B-I=1) color of the bulge (the different appearance is due to different gray scales).

The expected effect of scattering on colors is to render bluer the zones of an image where a substantial fraction of emerging radiation is contributed by forward scattering. This is due to the more asymmetric phase function at shorter  $\lambda$  (Sect. 2.2.2). This effect

should be more evident in highly inclined objects and in the regions of the (dust) disk situated between the observer and the bright bulge core (Elvius 1956).

Analyzing the pure bulge color maps we do note a less red lane near the center, coincident with the dust disk plane, but still with  $B-I \geq 1$ . This "blue" lane cannot be accounted for by scattering effects, since it is present also in models with absorption only. It is due, instead, to the heavy extinction of the central parts. Where this happens, the observed emission is mostly due to stars located out of the dust layer, and, therefore, the reddening is small. The reddest parts are in fact those where the local opacity (along the line of sight) is high but less than about 15. We note that when scattering is included, due to the lower effective opacity for a given  $\tau_V(0)$  this effect is reduced and the central equatorial lane actually becomes redder. The disk presents this lane as well, but the contrast is not so strong; as an example, we show in Fig. 7 the results along the major axis of a pure disk with  $\tau_V(0)=5$  at various inclinations: the right panel is for a model with scattering, while the left is for pure absorption. The study of the color profile has been suggested by BFK as a possible tool to infer the (local) optical depth: color gradients are located in regions where the optical depth along line of sight is  $\sim 1$ . Our models agree with this result. Besides, the shape of color profiles, and then the position of gradients, is about the same with or without scattering; this means that pure absorption models can provide sufficiently good  $\tau$  diagnostic.

EDITOR: PLACE FIGURE 7 HERE.

We have also performed simulations in U-band. Scattering effects in this wavelength are similar to those in the B-band and, therefore, U-B color maps are not appreciably different from those obtained with simpler absorption models.

## 4.2. Polarization analysis

We now examine the polarization properties of our models. The range of parameters explored is the same as for the surface brightness maps.

While the polarization introduced by a single scattering is usually conspicuous, it will be seen that the predicted degree of linear polarization is low (a few percent). This is due to three different causes:

1. Photons emerging from the same position in a map can be either *primitive*, unpolarized photons, emitted by stars and escaped without having been intercepted by dust, or scattered, polarized photons. The first cause of low polarization is, therefore, the dilution by primitive radiation, which is higher in the regions of higher surface brightness, such as the central parts of both bulges and disks.
2. If we restrict ourselves to the contribution to a certain pixel of scattered photons only, the resultant polarization will be maximum if the scattered photons have similar histories. So, the requirement for a high degree of polarization is threefold: first, the main contribution must come from single scattering events; second, photons must be scattered within a thin region along the line of sight; third, the scattering region must be illuminated from a narrow solid angle. The first and second requirements are usually met in the parameter range of our models. The third one requires a compact stellar distribution with respect to the dust disk and is only met by the bulge component.
3. The polarization will obviously be highest if the scattering grains are identical. As mentioned previously our models make use of a distribution of grains in size and composition, and to each size and composition our code assigns, for a given scattering angle, a different Mueller matrix. As a result, photons emitted by the same star and

scattered at the same point in the same direction may have quite different polarization properties, depending on the characteristics of the scattering grain.

The maps that we will examine are obtained by averaging the images for the various Stokes parameters within 10x10 pixel squares. This lower resolution has been necessary to compensate for the lower signal to noise figures of the polarization maps. In Fig. 8 are collected the linear polarization maps in the B-band at different inclinations for the emission from the bulge only, from the the disk only, and from a composite BT05 model. The disk of dust is the same in all cases, namely the one with highest optical depth,  $\tau_V(0) = 10$ .

EDITOR: PLACE FIGURE 8 HERE.

The degree of polarization comes out to be higher for larger optical depths. For the BT05 model of Fig. 8 at  $75^\circ$  inclination, the largest polarization degree is about 1.5%; in the same conditions but with  $\tau_V(0) = 0.5$  the maximum is 0.8%. The zones of highest polarization are always located on, or near, the major axis. Another notable feature of our models is that, while increasing  $\tau_V(0)$  the location of the maximum polarization moves outward; this is illustrated by the sequences in Fig. 9. that show the behavior of the polarization degree along the major axis, with galactocentric distance for some of our models.

EDITOR: PLACE FIGURE 9 HERE.

Clearly, for the reasons discussed above, the main contribution comes from scattering of the radiation from the bulge. This component has a more compact distribution with an emissivity highly peaked at the center, which is seen by the scatterers in the disk almost as a point source. The case of a pure bulge best illustrates the dilution of polarization

by direct radiation; the maximum degree of polarization does not vary appreciably with inclination.

Pure disks show very little polarization when seen face-on; this fact is mainly due to the rather flat distribution of disk stars. The polarization degree increases with inclination, with a maximum around  $50^\circ$ - $80^\circ$  and then decreases again slightly, due to the long line of sight through the disk when approaching  $90^\circ$ . As a rule, in composite models the scattering of disk radiation will provide the polarization of the inner regions while the bulge will mainly polarize the external disk. Note how the strong polarization of the outer disk in case of a pure bulge ( $\approx 30\%$ ) is diluted by direct disk light and reduced to 1.0-1.5%. As a consequence, the morphology of the polarization pattern, when seen at favorable inclinations ( $50^\circ$ - $80^\circ$ ), is different in systems with different bulge luminosities: late spirals will have a more uniform elliptical pattern, and early ones a two lobe structure aligned along the major axis.

As for the direction of the linear polarization vector, it is invariably aligned perpendicularly to the major axis. This means that, for the scattered field, the  $\mathbf{E}$  component perpendicular to the plane of scattering  $\mathbf{E}_\perp$ , is higher than the parallel one  $\mathbf{E}_\parallel$  for most of the directions with a sizeable phase function. This is the situation commonly observed in scattering by small particles, where  $x = 2\pi a/\lambda \ll 1$ , as it is the case, for example, in electron scattering. When dealing with dust grains with refractive indexes around one, this is not the only possible situation. The pattern can be inverted, in principle, at larger values of  $x$ , see for example fig. 25 of Van de Hulst (1957). We have performed a few simulations to check if, with larger grains or at smaller  $\lambda$ , the pattern would appreciably change, in the sense of a polarization pattern with a definite alignment along the equator, when seen edge-on. Our results indicate that, for any reasonable dust composition and size distribution, this situation is difficult to achieve for  $\lambda \geq 2000 \text{ \AA}$ . The reason is that, at such

wavelengths, the scattered field is mainly contributed by graphite ( $\perp$ ) grains which have a (real) refractive index  $m \geq 2$ . This requires, for a radical change in the pattern direction, values of  $x \geq 1.5$ , which means, in the visual ( $\lambda = 5500\text{\AA}$ ), a lower cutoff  $a_- \geq 0.13\mu\text{m}$  instead of the canonical  $a_- = 0.005\mu\text{m}$ . The resulting polarization map for such a model is illustrated in Fig. 10 (note the low polarization degree).

EDITOR: PLACE FIGURE 10 HERE.

Another point to mention is the comparison between the polarization maps and the isophotal ones: two aspects are noticeable. First, although the brightest, inner parts show very little polarization, measurable values ( $> 1\%$ ) are diffuse over most of the galaxy image, well inside the 25 B-mag arcsec $^{-2}$ , and, therefore, accessible to observations (Fig. 11).

EDITOR: PLACE FIGURE 11 HERE.

Second, for a given model and inclination, we find little spatial correlation between extinction and polarization, even in highly inclined models with large  $\tau_V(0)$ ; for example, the equatorial dust lanes of highly inclined disks are not strongly polarized. This is another signature that polarization is mainly contributed by single scattering events in the outer layers of the disk.

A clear prediction of our models concerns the wavelength dependence of the degree of linear polarization, which we find to increase from the B to the I-band. This appears to be a general rule, independently of B/T ratios,  $\tau_V(0)$ , and inclination. Such effect is ascribed to the reduced extinction in the I-band and the subsequent increase of the number of single scatterings. Most of the effects mentioned above are clearly depicted in Fig. 7. The positions of the maxima coincide with regions where the local optical depth is  $\sim 1$ , similarly to what previously observed for color gradients.

If the number of scattering is larger than one, Mie scattering can in principle introduce a certain degree of local circular polarization. In all our model the circular polarization degree is contained within the noise level and never shows at levels higher than 0.1%.

## 5. Summary and conclusions

To study the extinction and polarization properties of dusty spiral galaxies, we have performed extensive Monte Carlo simulations using realistic galaxy models that include both a bulge and a disk component, simulating different Hubble types. The scattering properties are calculated from Mie’s theory for each dust grain; in addition, we follow the radiative transfer of the four Stokes parameters. The grains are assumed to be spherical, with a power-law size distribution, and consisting either of graphite or silicate. This enables us to produce both photometric and polarimetric maps of the galaxy for different optical depths, inclinations and B/T ratios; the main results derived from the analysis of such maps are summarized in the following.

In general, we find a very good agreement with the results of BFK, who used a series of approximations described above, concerning luminosity profiles, total extinction, isophote shapes and diameters.

We have shown that the overall effect of scattering (with respect to pure absorption) is to reduce the extinction for a given  $\tau_V(0)$ . Such decrement in the effective  $A_B$  is particularly evident in the central parts of bright bulges, as shown in Fig. 4, although the extinction fractional reduction is larger for late-type than for early-type spirals and increases with galactocentric distance. Sandwich models, often used in the literature, are shown to fail dramatically in reproducing the extinction - optical depth relation when scattering is properly considered, and they should not be used. From the analysis of the B-I color maps



we conclude that there is a net reddening of the galaxy due to dust even when scattering is included. In fact, the latter reduces on average the B-I color by about 0.1 mag, a mild but appreciable effect. Radial color gradients are found to exist in regions where the optical depth is of order unity.

The degree of linear polarization produced by scattering is usually small (of the order of a few percent), but still practically measurable. The reasons for this behavior are: (i) there is a dilution effect by direct stellar (unpolarized) radiation; (ii) scattering region is usually illuminated from a large solid angle, thus photons with different histories enter the same beam, and (iii) the distribution of grain sizes and materials degrades the coherence of the polarization. Most of the polarization comes from light from the bulge which is single scattered by the outer layers of the disk. This is not surprising, of course, since the bulge is more compact and resembles a point source. The polarization degree increases with the optical depth and with inclination, flattening out above  $\sim 80^\circ$ . The polarization pattern is found to be perpendicular to the major axis, independently of the morphology, inclination and optical depth; this result depends only on the optical properties of the dust grains, and can be reversed only by shifting to much larger radii the lower limit for the dust size.

It is interesting to note that some galaxies do show polarization patterns similar to those of our models (Scarrott, Rolph, & Semple 1990; Fendt et al. 1995). Among them, late type galaxies (NGC 5907, NGC 891) show polarization perpendicular to the major axis on the entire extent of the disk; early type galaxies (NGC 4594, NGC 4565), instead, show such polarization in the outer regions of the disk, whereas the central parts have polarization vectors consistent with dichroic absorption, that is parallel to the major axis. When polarization vectors are perpendicular to the major axis, the observed degree of linear polarization is about one percent, in agreement with our models.

Finally, there is little correlation between extinction and polarization degree and there

is a trend of increasing polarization from the B to the I band due to the reduced extinction in the I band and subsequent increase of single scatterings.

Part of this study has been supported by the Programma Vigoni. We acknowledge several stimulating discussions with R.-J. Dettmar, F. Menard, E. Landi degl’Innocenti and M. Landolfi. One of us (S. B.) wishes to thank the Arcetri Chaos team for useful suggestions.

### A. Description of the Monte Carlo code

With the Monte Carlo method each event in the photon life is determined by the probability distribution of a pseudo random variable,  $\rho(t)$ , that describes the statistical weight of the variable  $t$  in the event, and by extracting a random number  $R \in [0, 1]$ . The value  $t^*$  associated to the random number  $R$  according to  $\rho(t)$  is given by the general Monte Carlo formula

$$\frac{\int_{t_{min}}^{t^*} \rho(t) dt}{\int_{t_{min}}^{t_{max}} \rho(t) dt} = R \quad (\text{A1})$$

where  $t_{min}$  and  $t_{max}$  define the interval of possible values for  $t$ . In the following  $R_i$  will indicate a random number between 0 and 1.

As a standard reference frame we adopt a cartesian one, having the  $z$  axis along the galactic symmetry axis, the  $x$  and  $y$  axes on the equatorial plane. The  $y$  axis coincides with the nodal line (intersection between sky plane and equatorial plane).

## A.1. Emission

In our models photons are emitted by stars distributed in the galactic disk and bulge. The first step is to determine the coordinates of the star (i.e. the photon emission point) according to the star density distributions.

### A.1.1. Bulge emission

Using the Jaffe law, and substituting equation (2) in equation (A1), one finds a simple relation between the radial distance and a random number  $R_1$

$$\tilde{r}^* = r_b \frac{R_1}{\frac{n+1}{n} - R_1} \quad (\text{A2})$$

where  $n$  is the truncating factor of the Jaffe bulge and  $r_b$  the scale radius. The  $R^{1/4}$  and Jaffe distributions are relatively similar, but the relation between  $r_b$  and  $R_e$  depends on which physical parameters, and parts of the galaxy, we intend to match best. To our purpose, we need the relation fitting the luminosity within a given  $\tilde{r}$ , since this is the physical variable which we will directly associate with the Monte Carlo random numbers (this will be the case for the disk radial distribution as well). In this sense, when uniformly sampled over the luminosity content, the best correspondence between the two distributions is found for  $r_b = 1.16 R_e$ .

Then we determine the polar,  $\theta$ , and azimuthal,  $\phi$ , angles in spherical coordinates. With spherical symmetry we have:

$$\phi^* = 2\pi R_2, \quad \theta^* = \cos^{-1}(1 - 2R_3), \quad (\text{A3})$$

where  $R_2$  and  $R_3$  are two independent random numbers. Thus, the emission coordinates are

$$\begin{aligned} x_0 &= \tilde{r}^* \sin \theta^* \cos \phi^* \\ y_0 &= \tilde{r}^* \sin \theta^* \sin \phi^* \\ z_0 &= \tilde{r}^* \cos \theta^*. \end{aligned} \tag{A4}$$

In the more general case of axially symmetric ellipsoids,  $z_0$  becomes

$$z_0 = \tilde{r}^* \epsilon \cos \theta^* \tag{A5}$$

where  $\epsilon$  is the ratio between the minor and major axis.

#### A.1.2. Disk emission

For an exponential disk (eq. [3]), the cylindrical radius of emission  $r^*$  can be found inverting numerically

$$\frac{\int_0^{r^*} e^{-\frac{r}{r_d}} r dr}{\int_0^{r_{max}} e^{-\frac{r}{r_d}} r dr} = \frac{1 - (1 + t^*)e^{-t^*}}{1 - (1 + m)e^{-m}} = R'_1 \tag{A6}$$

with  $t^* = r^*/r_d$ . From the azimuthal symmetry around the  $z$  axis:

$$\phi^* = 2\pi R'_2. \tag{A7}$$

We calculate  $z$  using

$$\frac{\int_{-z_{max}}^{z^*} Z\left(\frac{z}{z_d}\right) dz}{\int_{-z_{max}}^{z_{max}} Z\left(\frac{z}{z_d}\right) dz} = R'_3 \tag{A8}$$

where

$$Z\left(\frac{z}{z_d}\right) = \begin{cases} \exp(-|z|/z_d), \\ \operatorname{sech}^2(z/z_d). \end{cases} \tag{A9}$$

For the exponential law, we have

$$t^* = -\operatorname{sgn}\left(R'_3 - \frac{1}{2}\right) \ln \left[ \operatorname{sgn}\left(R'_3 - \frac{1}{2}\right) (1 - 2R'_3) (1 - e^{-k}) + 1 \right]; \tag{A10}$$

for the  $\text{sech}^2$  law, the relation is

$$t^* = \tanh^{-1} \{2 [\tanh(k)] R'_3 - \tanh(k)\}, \quad (\text{A11})$$

where  $t^* = z^*/z_d$  and  $k$  is the vertical truncation factor. Thus

$$\begin{aligned} x_0 &= r^* \cos \phi^* \\ y_0 &= r^* \sin \phi^* \\ z_0 &= z^*. \end{aligned} \quad (\text{A12})$$

### A.1.3. Direction

If the radiation is emitted isotropically by stars, the longitude and colatitude of its direction are

$$\phi = 2\pi R_4, \quad \theta = \cos^{-1}(1 - 2R_5), \quad (\text{A13})$$

from which the direction cosines are computed

$$\begin{aligned} l_0 &= \sin \theta \cos \phi \\ m_0 &= \sin \theta \sin \phi \\ n_0 &= \cos \theta. \end{aligned} \quad (\text{A14})$$

We define the unit vector  $\mathbf{v}_0 \equiv (l_0, m_0, n_0)$ .

The stellar radiation is largely unpolarized, so we will assume for the initial Stokes parameters

$$\begin{pmatrix} I_0 \\ Q_0 \\ U_0 \\ V_0 \end{pmatrix} = \begin{pmatrix} 1 \\ 0 \\ 0 \\ 0 \end{pmatrix}. \quad (\text{A15})$$

In the following the Stokes parameters will be calculated assuming as reference direction the projection of the  $z$  axis on the plane normal to the photon direction (for unpolarized radiation equation [A15] is true in all reference frames).

In summary, for the emission of every photon, we need to extract five random numbers, three for the coordinates of the point of emission and two for the direction of emission.

## A.2. Diffusion point

A photon emitted in  $(x_0, y_0, z_0)$  along the direction  $\mathbf{v}_0$  travels undisturbed until it collides with a dust grain. If undisturbed, the geometrical path within the dust distribution would be:

$$\Gamma(t) = \begin{cases} x = x_0 + l_0 t \\ y = y_0 + m_0 t \\ z = z_0 + n_0 t \end{cases} \quad 0 \leq t < t_T \quad (\text{A16})$$

where  $t_T$  is the t-value corresponding to the point of exit from the dust disk. The total optical depth  $\tau_T$  along this path is

$$\tau_T = \frac{\tau_\lambda(0)}{2z_g} \int_0^{t_T} \frac{\rho^{(g)}(r, z)}{\rho_0^{(g)}} dt \quad (\text{A17})$$

where we made use of equation (6), and  $r = \sqrt{x^2 + y^2}$ . A fraction  $e^{-\tau_T}$  of the photons will then emerge undisturbed from the system, while the remaining  $1 - e^{-\tau_T}$  will be absorbed or diffused in other directions. The point of diffusion is associated with a random number  $R_6$ , which determines the total optical depth at the diffusion point according to

$$\int_0^\tau e^{-\xi} d\xi = R_6, \quad (\text{A18})$$

or

$$\tau = -\ln(1 - R_6). \quad (\text{A19})$$

If  $\tau$  is greater than  $\tau_T$ , the photon will exit without scattering. This procedure, however, is quite inefficient: if  $\tau_T$  is small, most of the photons will exit directly. To overcome this problem, we have used the method of *forced scattering* introduced by Cashwell & Everett (1959; see also Witt 1977). With this method the photon is split into two components:

one, with intensity  $I_1 = \exp(-\tau_T)$ , keeps travelling undisturbed and exits the dust disk, the other, with intensity  $I_2 = 1 - \exp(-\tau_T)$  is forced to scatter. Accordingly, equations (A18) and (A19) become

$$\frac{\int_0^\tau e^{-\xi} d\xi}{\int_0^{\tau_T} e^{-\xi} d\xi} = R_6. \quad (\text{A20})$$

and

$$\tau = -\ln(1 - R_6(1 - e^{-\tau_T})), \quad (\text{A21})$$

respectively. In the limit  $\tau_T \rightarrow \infty$ ,  $\tau$  tends to the value for unforced scattering. The other Stokes parameters are scaled accordingly. Forcing the scattering has also the effect of reducing the noise in the resulting images, for the same total number of photons launches, but it is appreciably more time consuming. We performed a series of trial simulations using a point source embedded in spherical envelopes of optical opacity from 1 to 10. As a result of these tests, we adopted the following scheme in our code: the first scattering is always forced; the following ones are forced only if  $\tau_T > 1$ . Among the various tested schemes, this one attains the best S/N ratio within a given computational time.

We have used a threshold value  $\tau_{lim}$  for the optical depth: if a photon travels along a path with  $\tau_T < \tau_{lim}$  it is allowed to escape without being attenuated; the adopted value is  $\tau_{lim} = 10^{-4}$ . Once  $\tau$ , the optical depth of the impact event, has been calculated, the integral in equation (A17), but with  $t_1$  instead of  $t_T$ , is inverted to find the value of  $t_1$ , the geometrical length travelled before impact. The coordinates of the first scattering are then

$$\begin{aligned} x_1 &= x_0 + l_0 t_1 \\ y_1 &= y_0 + m_0 t_1 \\ z_1 &= z_0 + n_0 t_1. \end{aligned} \quad (\text{A22})$$

### A.3. Choice of the dust grain

We now need to know the geometrical and optical characteristics of the dust particle located at  $x_1, y_1, z_1$ . The probability for a photon to collide with a spherical grain of radius  $a$ , refractive index  $m$ , and material  $i$ , is proportional to the product of the extinction cross section,  $C_i^{ext}$ , and the grain number density  $n(a) \propto a^{-3.5}$  (MRN model). The differential collision probability can be written as

$$dP_i(a) \propto w_i a^{-3.5} C_i^{ext} da, \quad (\text{A23})$$

where  $w_i$  is the statistical weight of material  $i$ . Let us call  $\chi_i(a)$  the function

$$\chi_i(a) = \int_{a_-}^a dP_i(a) \quad a \in [a_-, a_+].; \quad (\text{A24})$$

$\chi_i(a)$  can be normalized to unity dividing it by the value  $\chi_{tot}(a_+) = \sum_i \chi_i(a_+)$ :

$$\bar{\chi}_i(a) = \frac{\chi_i(a)}{\chi_{tot}(a_+)}. \quad (\text{A25})$$

$\bar{\chi}_i(a)$  has now values between 0 and  $\bar{\chi}_i(a_+)$ . The interval  $[0, 1]$  can be divided in three subintervals for the three materials (Si, C $\parallel$ , C $\perp$ )

$$[0, \bar{\chi}_{\text{Si}}(a_+)],$$

$$[\bar{\chi}_{\text{Si}}(a_+), \bar{\chi}_{\text{Si}}(a_+) + \bar{\chi}_{\text{C}\parallel}(a_+)], \quad (\text{A26})$$

$$[\bar{\chi}_{\text{Si}}(a_+) + \bar{\chi}_{\text{C}\parallel}(a_+), 1].$$

In this way, by means of a random number  $R_7$  we choose both the grain material and size.

The grain size is found inverting the integral

$$\int_{a_-}^a \bar{\chi}_i(a) da + B_i = R_7, \quad (\text{A27})$$



where  $B_i$  is the value associated with the minimum value of each subinterval ( $B_{\text{Si}} = 0$ ,  $B_{\text{C}\parallel} = \bar{\chi}_{\text{Si}}(a_+)$ , etc.). By knowing the wavelength and the material, we determine the complex refractive index, which, together with size, characterizes completely the optical properties of the grain.

#### A.4. Scattering direction and polarization transfer

If  $\mathbf{v}_0$  and  $\mathbf{v}_1$  are unit vectors defining the propagation direction before and after scattering, respectively, we define  $\mathbf{p}_{z0}$  as the unit vector indicating the projection of the positive  $z$  axis (the galactic symmetry axis specified by the unit vector  $\mathbf{k}$ ) onto the plane perpendicular to  $\mathbf{v}_0$  at the scattering point. As mentioned before,  $\mathbf{p}_{z0}$  defines the reference direction for the Stokes parameters of the incoming photon.

Two angles define  $\mathbf{v}_1$  with respect to  $\mathbf{v}_0$  (Fig. 12): the polar angle,  $\theta$ , between  $\mathbf{v}_0$  e  $\mathbf{v}_1$ , which is the actual angle of scattering, and the azimuthal angle,  $\phi$ , between  $\mathbf{p}_{z0}$  and  $\mathbf{s}_0$  the projection of  $\mathbf{v}_1$  on the plane normal to  $\mathbf{v}_0$ . The vector  $\mathbf{s}_0$  also lies in the scattering plane defined by  $\mathbf{v}_0$  and  $\mathbf{v}_1$ .

EDITOR: PLACE FIGURE 12 HERE.

After some algebra we derive

$$\mathbf{p}_{z0} = \frac{1}{\sqrt{1 - n_0^2}} (-l_0 n_0, -m_0 n_0, 1 - n_0^2) \quad (\text{A28})$$

Since the Mueller matrix elements are more easily defined for Stokes parameters referred to the scattering plane, we first have to perform a rotation about  $\mathbf{v}_0$  and change to  $\mathbf{s}_0$  the reference direction. The Stokes parameters of the incoming photon referred to the

scattering plane are then

$$\begin{pmatrix} I'_0 \\ Q'_0 \\ U'_0 \\ V'_0 \end{pmatrix} = \begin{pmatrix} 1 & 0 & 0 & 0 \\ 0 & \cos 2\phi & \sin 2\phi & 0 \\ 0 & -\sin 2\phi & \cos 2\phi & 0 \\ 0 & 0 & 0 & 1 \end{pmatrix} \begin{pmatrix} I_0 \\ Q_0 \\ U_0 \\ V_0 \end{pmatrix} \quad (\text{A29})$$

With our assumptions, the phase function for polarized radiation is (van de Hulst 1957, pg. 15)

$$\begin{aligned} \Phi(\theta, \phi) &= \frac{1}{\pi x^2 Q^{sca}} \left[ S_{11} + S_{12} \frac{Q'_0}{I'_0} \right] \\ &= \frac{1}{\pi x^2 Q^{sca}} \left[ S_{11}(\theta) + S_{12}(\theta) \left( \frac{Q_0}{I_0} \cos 2\phi + \frac{U_0}{I_0} \sin 2\phi \right) \right]. \end{aligned} \quad (\text{A30})$$

where

$$x = \frac{2\pi a}{\lambda}, \quad Q^{sca} = \frac{C^{sca}}{\pi a^2}. \quad (\text{A31})$$

$S_{11}$  and  $S_{12}$  are two elements of the Mueller matrix, which are functions only of  $\theta$  (spherical grains), and  $C^{sca}$  is the scattering cross section (analogous to  $C^{ext}$ ). The angles  $\theta$  e  $\phi$  are distributed according to equation (A30). The phase function,  $\Phi$ , is normalized, so that

$$1 = \int_0^{2\pi} d\phi \int_0^\pi d\theta \sin \theta \Phi(\theta, \phi) = \int_0^\pi d\theta \sin \theta \tilde{\Phi}(\theta) \quad (\text{A32})$$

where  $\tilde{\Phi}$  is

$$\tilde{\Phi}(\theta) = \int_0^{2\pi} \Phi(\theta, \phi) d\phi = \frac{2}{x^2 Q^{sca}} S_{11}(\theta); \quad (\text{A33})$$

$\tilde{\Phi}$  depends only on  $\theta$  so that  $\theta$  can be derived from the Monte Carlo method, independently both of  $\phi$  and of the polarization of the incident radiation. The scattering polar angle,  $\bar{\theta}$ , can be calculated from a random number  $R_8$ , inverting

$$\int_0^{\bar{\theta}} \tilde{\Phi}(\theta) \sin \theta d\theta = R_8. \quad (\text{A34})$$

Substituting this value of  $\bar{\theta}$  in equation (A30) we can find  $\bar{\phi}$ , from

$$\frac{\int_0^{\bar{\phi}} \Phi(\bar{\theta}, \phi) d\phi}{\int_0^{2\pi} \Phi(\bar{\theta}, \phi) d\phi} = R_9, \quad (\text{A35})$$

or

$$\frac{1}{2\pi} \left[ \bar{\phi} + \frac{S_{12}(\bar{\theta})}{2S_{11}(\bar{\theta})} \left( \frac{Q_0}{I_0} \sin 2\bar{\phi} + \frac{U_0}{I_0} (1 - \cos 2\bar{\phi}) \right) \right] = R_9. \quad (\text{A36})$$

Using the values of  $\bar{\theta}$  and  $\bar{\phi}$  obtained before, we compute the direction cosines of  $\mathbf{v}_1$

$$\begin{aligned} l_1 &= \frac{\sin \bar{\theta}}{\sqrt{1 - n_0^2}} \left( -l_0 n_0 \cos \bar{\phi} + m_0 \sin \bar{\phi} \right) + l_0 \cos \bar{\theta} \\ m_1 &= \frac{-\sin \bar{\theta}}{\sqrt{1 - n_0^2}} \left( m_0 n_0 \cos \bar{\phi} + l_0 \sin \bar{\phi} \right) + m_0 \cos \bar{\theta} \\ n_1 &= \sqrt{1 - n_0^2} \sin \bar{\theta} \cos \bar{\phi} + n_0 \cos \bar{\theta}. \end{aligned} \quad (\text{A37})$$

The new direction of propagation allow us to calculate the updated Stokes parameters after scattering (but still referred to the scattering plane) by applying the Mueller matrix

$$\begin{pmatrix} I_1'' \\ Q_1'' \\ U_1'' \\ V_1'' \end{pmatrix} = \begin{pmatrix} S_{11} & S_{12} & 0 & 0 \\ S_{12} & S_{11} & 0 & 0 \\ 0 & 0 & S_{33} & S_{34} \\ 0 & 0 & -S_{34} & S_{33} \end{pmatrix} \begin{pmatrix} I_0' \\ Q_0' \\ U_0' \\ V_0' \end{pmatrix}. \quad (\text{A38})$$

It will be noted that equation (A38) is different from the usual relation for the scattered Stokes vector, since it does not include the spherical factor  $1/k^2 r^2$ . The standard formulae (e.g. Bohren & Huffman 1983, eq. [3.16]) are derived for the distribution of the scattered electromagnetic fields, within the frame of the electromagnetic theory. In our description, the scattered photon is not distributed over the entire solid angle but, instead, deflected onto a new single direction, and attenuated by a factor equal to the albedo (which in

Mie’s approximation is independent of direction). If  $I'_1$  is the correct value of the scattered intensity, we have:

$$I'_1 = \tilde{\omega}I'_0 = \tilde{\omega}I_0, \quad (\text{A39})$$

and the correct value of the Stokes vector after scattering will be

$$\begin{pmatrix} I'_1 \\ Q'_1 \\ U'_1 \\ V'_1 \end{pmatrix} = \frac{\tilde{\omega}I_0}{I'_1} \begin{pmatrix} I''_1 \\ Q''_1 \\ U''_1 \\ V''_1 \end{pmatrix}. \quad (\text{A40})$$

The new Stokes parameters are defined with respect to  $\mathbf{s}_1$ , the unit vector which lies in the scattering plane and in the plane perpendicular to the new direction of propagation  $\mathbf{v}_1$  (Fig. 13): coherently with the convention adopted, we now have to calculate the Stokes parameters using, as a reference,  $\mathbf{p}_{z1}$  the projection of the  $z$  axis onto the plane normal to  $\mathbf{v}_1$ .

EDITOR: PLACE FIGURE 13 HERE.

The expression for  $\mathbf{p}_{z1}$  is analogous to that for  $\mathbf{p}_{z0}$ , provided we substitute  $\mathbf{v}_1$ , for  $\mathbf{v}_0$ . Since  $\mathbf{s}_1$  lies in the scattering plane, it is parallel to the projection of  $\mathbf{v}_0$  onto the plane normal to  $\mathbf{v}_1$  (but with opposite direction), and we have

$$\mathbf{s}_1 \times (\mathbf{v}_0 - (\mathbf{v}_0 \cdot \mathbf{v}_1)\mathbf{v}_1) = 0 \quad (\text{A41})$$

From the previous relation we have

$$\mathbf{s}_1 = \frac{1}{\sqrt{1 - (\mathbf{v}_0 \cdot \mathbf{v}_1)^2}} (l_1(\mathbf{v}_0 \cdot \mathbf{v}_1) - l_0, m_1(\mathbf{v}_0 \cdot \mathbf{v}_1) - m_0, n_1(\mathbf{v}_0 \cdot \mathbf{v}_1) - n_0) \quad (\text{A42})$$

The angle  $\gamma$  between  $\mathbf{p}_{z1}$  and  $\mathbf{s}_1$  is found using two other relations:

$$\cos \gamma = \mathbf{p}_{z1} \cdot \mathbf{s}_1 = \frac{n_1(\mathbf{v}_0 \cdot \mathbf{v}_1) - n_0}{\sqrt{1 - n_1^2} \sqrt{1 - (\mathbf{v}_0 \cdot \mathbf{v}_1)^2}} \quad (\text{A43})$$

$$\sin \gamma \mathbf{v}_1 = \mathbf{p}_{z1} \times \mathbf{s}_1 = \frac{m_0 l_1 - l_0 m_1}{\sqrt{1 - n_1^2} \sqrt{1 - (\mathbf{v}_0 \cdot \mathbf{v}_1)^2}} \mathbf{v}_1. \quad (\text{A44})$$

The Stokes parameters referred to  $\mathbf{p}_{z1}$  will be calculated applying a rotation by an angle  $(-\gamma)$

$$\begin{pmatrix} I_1 \\ Q_1 \\ U_1 \\ V_1 \end{pmatrix} = \begin{pmatrix} 1 & 0 & 0 & 0 \\ 0 & \cos 2\gamma & -\sin 2\gamma & 0 \\ 0 & \sin 2\gamma & \cos 2\gamma & 0 \\ 0 & 0 & 0 & 1 \end{pmatrix} \begin{pmatrix} I'_1 \\ Q'_1 \\ U'_1 \\ V'_1 \end{pmatrix} \quad (\text{A45})$$

In summary, every diffusion event requires four random numbers, one to locate the diffusion point, one for the optical characteristics of the grain and two to determine the new direction of propagation.

### A.5. Imaging

After  $N$  scatterings, the photon parameters satisfy the exit conditions. The final parameters are the point of last scattering,  $x_N, y_N, z_N$ , the exit direction,  $\mathbf{v}_N = (l_N, m_N, n_N)$ , and the exit Stokes parameters,  $I_N, Q_N, U_N, V_N$ .

Our galactic models have two simmetries that can be used to reduce the computational time: (i) axial simmetry around the  $z$  axis and (ii) planar simmetry about the equatorial ( $xy$ ) plane. If we look at the galaxy from a point at infinite distance in the  $xz$  plane, given the axial simmetry, we perform a rotation around the  $z$  axis and align  $\mathbf{v}_n$  parallel to the  $xz$  plane. After rotation, the exit direction can be identified by the new coordinates of the point of last scattering  $(x, y, z)$  and by the polar angle  $\theta$  only (we omit pedix N for simplicity). The corresponding Stokes parameters  $(I, Q, U, V)$  will be the same as  $I_n, Q_n, U_n, V_n$  because a rotation around the  $z$  axis does not modify the relative orientation of the wave electric field and the  $z$  axis. Because of the axial simmetry, for each photon exiting from  $(x, y, z)$  with

direction  $\theta$  and parameters (I,Q,U,V) we can add another photon exiting from  $(x,-y,z)$  with the same direction and parameters (I,Q,-U,-V). We can then exploit the planar symmetry: for each photon exiting from  $(x,y,z)$  with direction given by  $\theta$  and parameters (I,Q,U,V) we add a photon with  $(x,y,-z)$ , direction  $\pi - \theta$  and parameters (I,Q,-U,-V). Using these symmetries we gain, therefore, a factor four in the number of photons.

To produce maps of the galaxy as seen from different inclinations we select the photons, after their exit, according to their  $\theta$  direction. This is done by dividing the whole solid angle in  $N_b$  latitudinal bands, of equal solid angle. All the photons with exit direction within a given band will contribute to the image relative to that range of  $\theta$  values. Note that this introduces a finite resolution in inclination: for example with our standard ( $N_B=15$ ) sampling, the most face-on image includes inclinations ranging from  $0^\circ$  to  $30^\circ$ , while the edge-on case includes inclinations between  $86^\circ$  and  $94^\circ$ . Having already exploited the planar symmetry, images with inclination  $\theta$  and  $\pi - \theta$  will be identical. Finally, the photons pertaining to a certain inclination band are projected onto the plane of the sky, according to their point of last scattering and direction.

The final result consists of  $N_B$  images for each Stokes parameter. Linear polarization maps are obtained calculating, for each pixel, the linear polarization,

$$P = \frac{\sqrt{Q^2 + U^2}}{I}, \quad (\text{A46})$$

and the polarization angle,

$$\psi = \frac{1}{2} \text{atan} \frac{U}{Q} + \psi_0 \quad (\text{A47})$$

where  $\psi_0$  is defined in Calamai, Landi degl’Innocenti, & Landi degl’Innocenti (1975).

## REFERENCES

- Bianchi, S. 1995, Laurea Thesis, University of Florence
- Block, D. L., Witt, A. N., Grosbøl, P., Stockton, A., & Moneti, A. 1994, *A&A*, 288, 383
- Bohren, C. F., & Huffman, D. R. 1983, *Absorption and Scattering of Light by Small Particles* (New York: Wiley)
- Burstein, D., Haynes, M. P., & Faber, S. M. 1991, *Nature*, 353, 515
- Byun, Y. I., Freeman, K. C., & Kylafis, N. D. 1994, *ApJ*, 432, 114 (BFK)
- Calamai, G., Landi degl’Innocenti, E., & Landi degl’Innocenti, M. 1975, *A&A*, 45, 297
- Cashwell, E.D., & Everett, C.J. 1959, *A Practical Manual on the Monte Carlo Method for Random Walk Problems* (New York: Pergamon)
- Chołoniewski, J., 1991, *MNRAS*, 239, 939
- de Vaucouleurs, G., 1959, In *Handbuch der Physik*, Vol. 53, (Berlin: Springer-Verlag)
- de Vaucouleurs, G., de Vaucouleurs, A., Corwin, H. G., Buta, R. J., Pature, G. & Forqué, P. 1991, *Third Reference Catalogue of Bright Galaxies* (New York: Springer)
- Disney, M. J., Davies, J. I., & Phillipps, S. 1989, *MNRAS*, 239, 939
- Draine, B. T., & Lee, H. M. 1984, *ApJ*, 285, 89
- Elvius, A. 1956, *Stockholm Obs. Ann.*, 18, N. 9
- Evans, R. 1994, *MNRAS*, 266, 511
- Fendt, C., Beck, R., Lesch, H., & Neininger, N. 1995, *A&A*, in press
- Fischer, O., Henning, Th., & Yorke, H.W. 1994, *A&A*, 284, 187
- Freeman, K. C. 1970, *ApJ*, 160, 811
- Giovanelli, R., Haynes, M. P., Salzer, J. J., Wegner, G., da Costa, L. N. D., & Freudling, W. 1994, *AJ*, 107, 2036

- Gledhill, T. M., & Scarrott, S. M. 1989, MNRAS, 236, 139
- Henry, L. G., & Greenstein, J. L. 1941, ApJ, 93, 70
- Holmberg, E. 1958, Medd. Lunds Astron. Obs., Ser. II, Nr. 136
- Jaffe, W. 1983, MNRAS, 202, 995
- Kylafis, N. D., & Bahcall, J. M. 1987, ApJ, 317, 637
- Martin, P. G., & Rouleau, F. 1991, Extreme Ultraviolet Astronomy, ed. Malina, R. F., Bowyer, S.
- Mathis, J. S., Ruml, W., & Nordsieck, K.H. 1977, ApJ, 217, 425 (MRN)
- Menard, F. 1989, PhD Thesis, University of Montreal
- Ohta, K., & Kodaira, K. 1995, PASJ, 47, 17
- Peletier, R. F., Valentijn, E. A., Moorwood, A. F. M., & Freudling, W. 1994, A&AS, 108, 621
- Rieke, G. J., & Lebofsky, M. J. 1985, ApJ, 288, 618
- Sandage, A. & Tammann, G. A., 1981, A Revised Shapley-Ames Catalog of Bright Galaxies, (Washington D.C.: Carnegie)
- Scarrott, S. M., Rolph, C. D., & Semple, D. P. 1990, Proc. IAU Symp. 140, 254
- Shurcliff, W., A. 1962, Polarized light, (Harvard University press)
- Spitzer, L. 1978, Physical processes in the Interstellar Medium, (New York: Wiley)
- Valentijn, E. A. 1990, Nature, 346, 153
- Valentijn, E. A. 1994, MNRAS, 266, 614
- van de Hulst, H. C. 1957, Light Scattering by small particles, (New York: Dover)
- van der Kruit, P. C., & Searle, L. 1981, A&A, 95, 105



Wainscoat, R. J., Freeman, K., & Hyland, A. R. 1989, *ApJ*, 337, 163

Wielebinski, R., & Krause, F. 1993, *A&A Rev.*, 4, 449

Witt, A. N., 1977, *ApJS*, 35, 1

Young , P. J. 1976, *AJ*, 81, 807

Fig. 1.— The extinction curve resulting from the adopted dust model. Also shown are the contributions of the single components. The color excesses for the single materials are divided by the value of  $E(B-V)$  for the total mixture.

Fig. 2.— Average phase functions as computed by the Monte Carlo code (solid lines) and HG phase functions with  $g$  corresponding to the mean value for the same dust distribution (dashed lines); the phase functions are shown at the central wavelength of the B and I bandpasses.

Fig. 3.— Difference in B total magnitude between models including scattering,  $B_T(sc)$ , and with absorption only,  $B_T(abs)$ , as a function of inclination, for different bulge/total ratios. In each panel the five lines refer to different total opacities:  $\tau_V(0) = 10, 5, 2, 1, 0.5$ , from top to bottom.

Fig. 4.— Central ( $r = 0$ ) extinction versus optical depth  $\tau_V(0)$  for B models with  $i = 20^\circ$  (solid lines); left panel is for models with absorption only, right panel for absorption + scattering models. Dotted lines refer to sandwich models with different dust-to-starthickness ratios ( $\xi$ ). The straight solid line is for the screen model.

Fig. 5.— As in Fig. 4, but for  $r = r_d$ .

Fig. 6.— B band images (left) and B-I color maps (right) for a bulge (top), a disk (center) and a BT05 model (bottom) as seen from an inclination of  $82^\circ$ . The dust disk is the same in the three cases, with  $\tau_V(0) = 10$ .

Fig. 7.— Color profiles along the major axis for a BT00 model (pure disk) with  $\tau_V(0) = 5$  at various inclinations. Left panel is for models with only absorption, the right one for absorption+scattering model. Lines are truncated at  $r = 4r_d$  because of the poor S/N at larger radii.

Fig. 8.— B-band polarization maps for a bulge (top), a disk (middle), and a BT05 model (bottom). The optical depth is  $\tau_V(0) = 10$  and the inclinations  $20^\circ, 75^\circ, 90^\circ$  (from left to right). The dust disk is the same in the three cases. For each model, the linear polarization scale is given on the right. The dashed circle in the upper maps corresponds to the extent of the bulge.

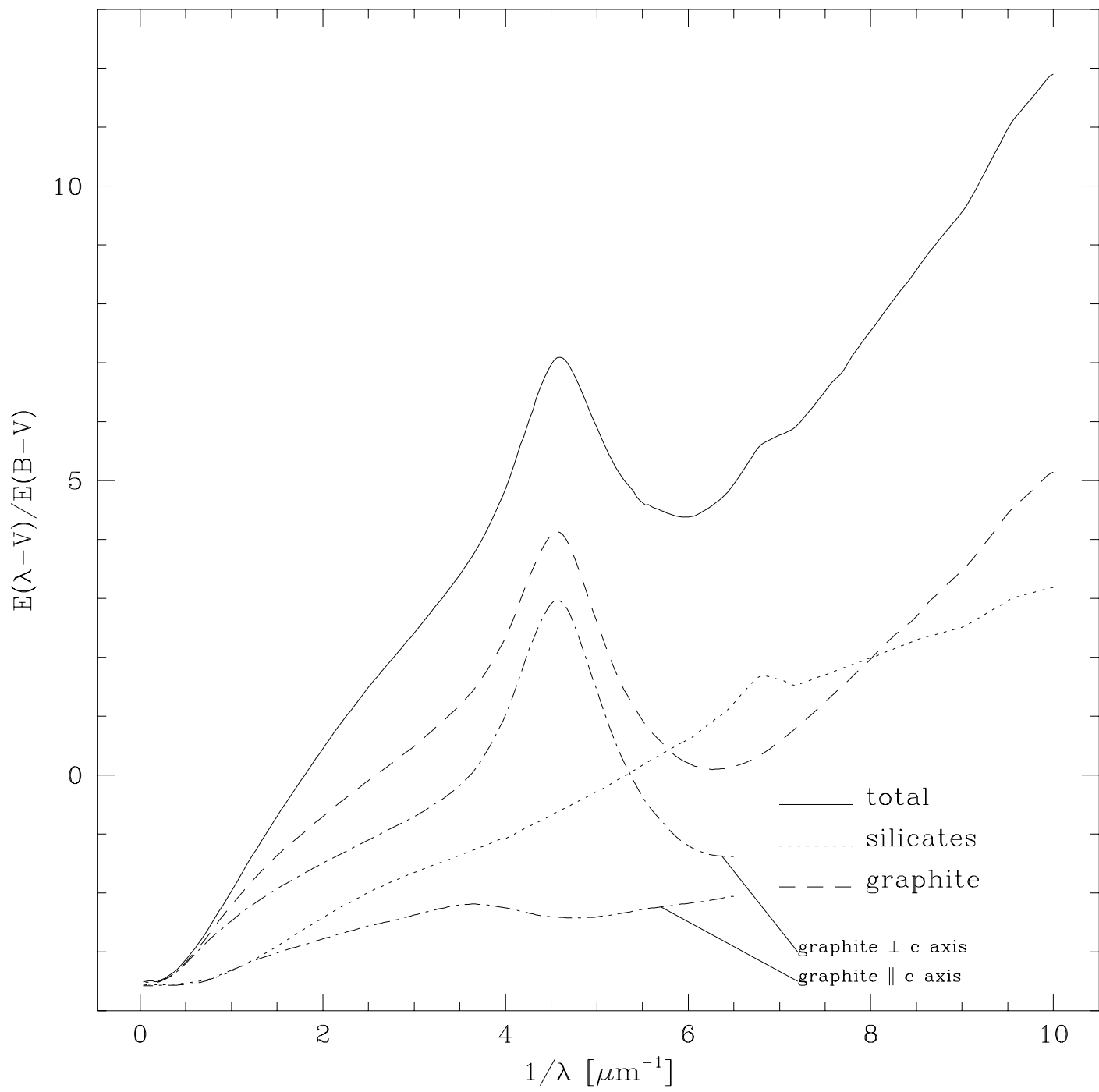
Fig. 9.— Linear polarization profiles along the major axis for BT05 models at inclinations  $20^\circ, 75^\circ, 90^\circ$ , for B-band (left) and I-band (right). Profiles for  $\tau_V(0) = 0.5, 2, 10$  are plotted.

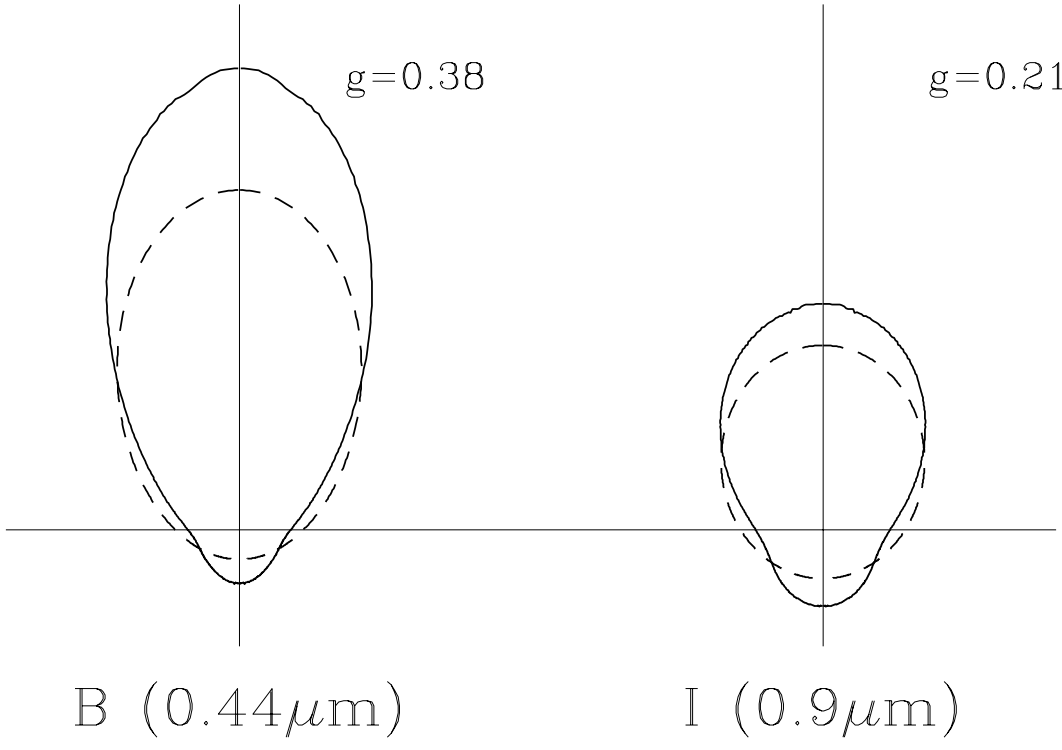
Fig. 10.— B-band BT05 model seen from  $75^\circ$ , with  $\tau_B(0) = 5$  and a lower grain size cutoff  $a_- = 0.15\mu\text{m}$ ; coordinates are measured in units of  $r_d$ .

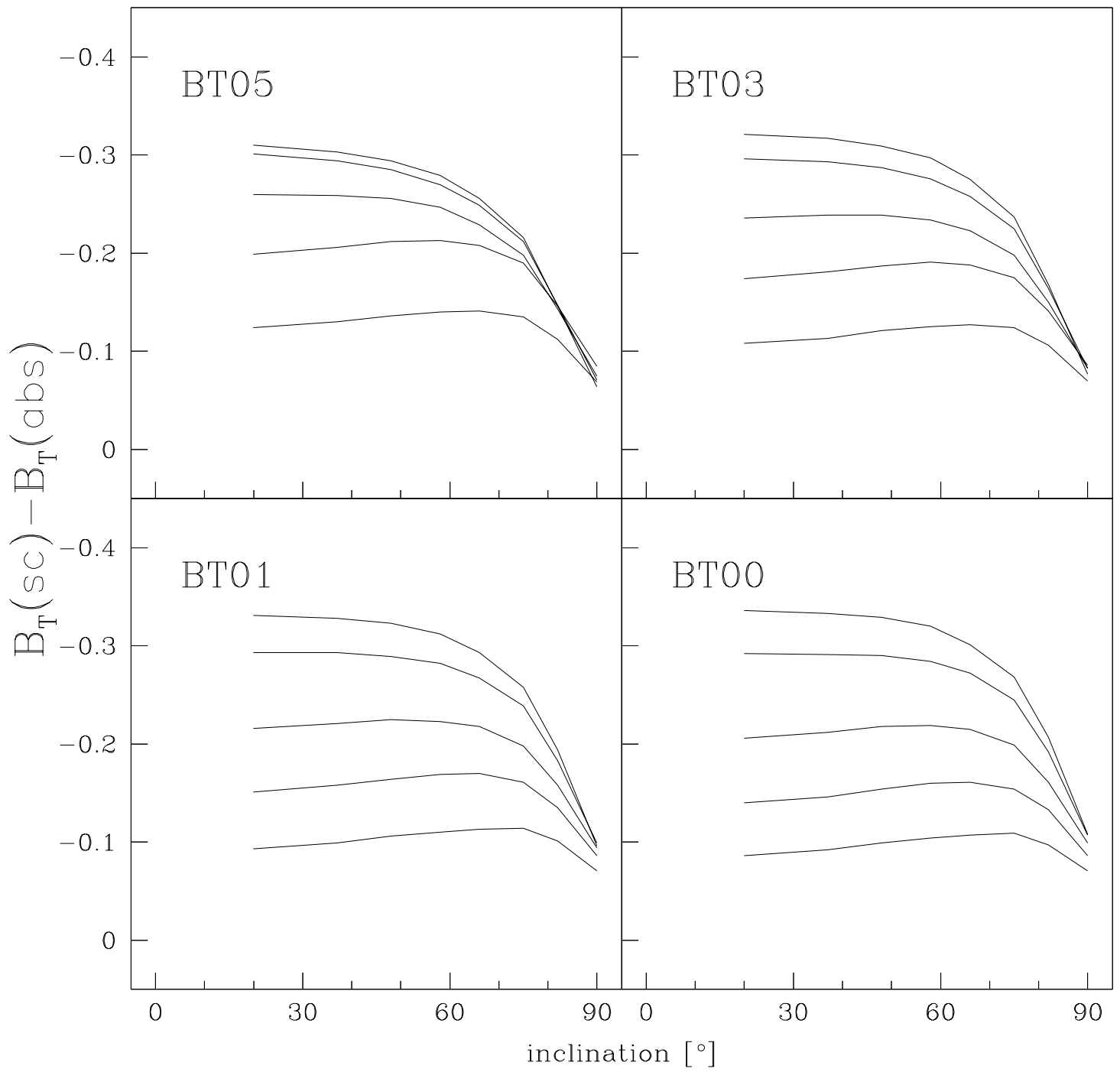
Fig. 11.— B-band polarization maps for a BT05 model, with  $\tau_V(0) = 10$ , for inclinations  $i = 75^\circ$  (left) and  $i = 82^\circ$  (right). Isophotes up to 25 B-mag arcsec $^{-2}$  are superimposed, spaced by 1 mag. The assumed face-on disk central brightness is 21.6 B-mag arcsec $^{-2}$  (Freeman 1970).

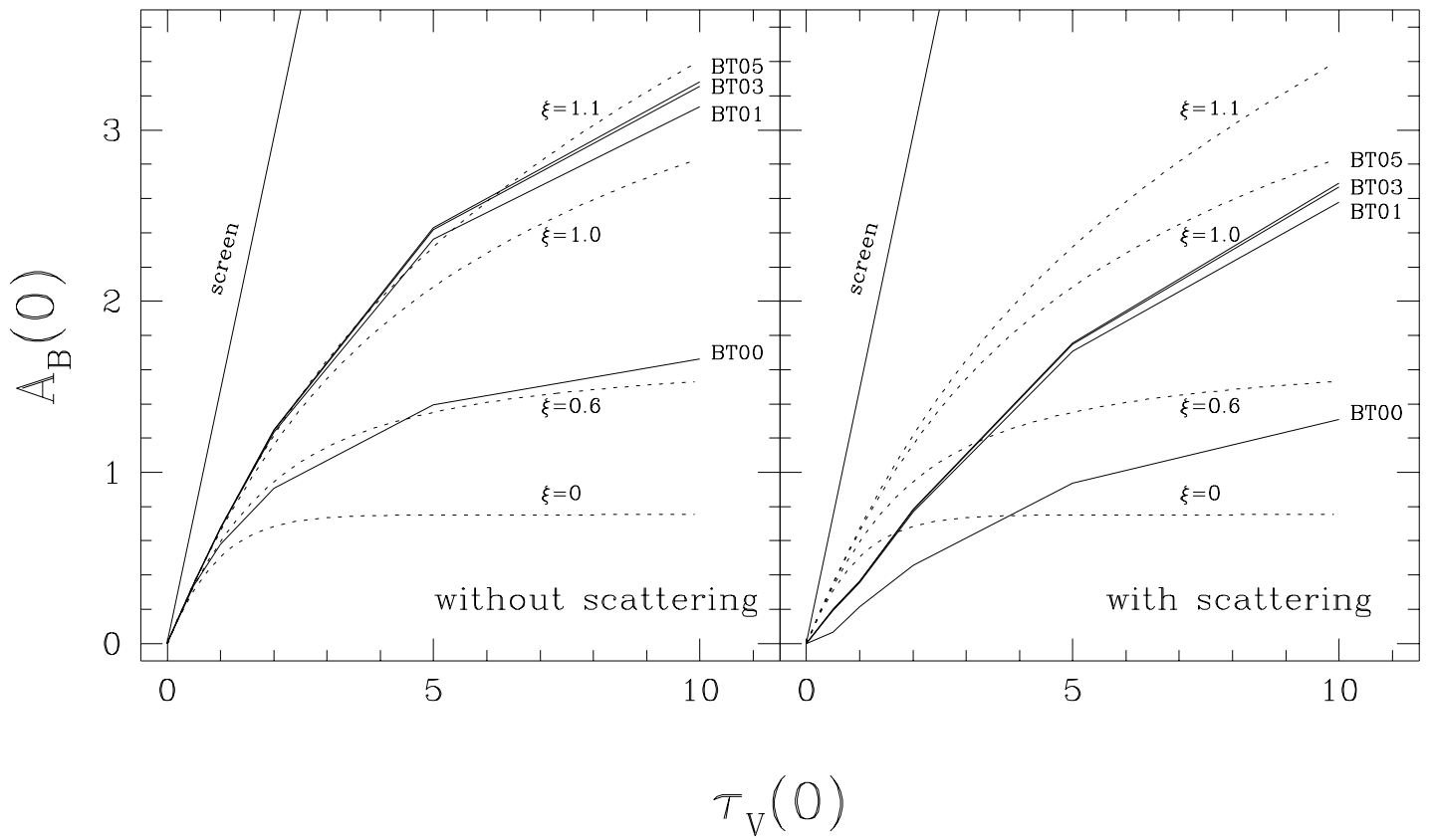
Fig. 12.— Scattering geometry:  $\mathbf{v}_0$  is the original direction of the photon and  $\mathbf{v}_1$  the direction after scattering; the other vectors are defined in the text.

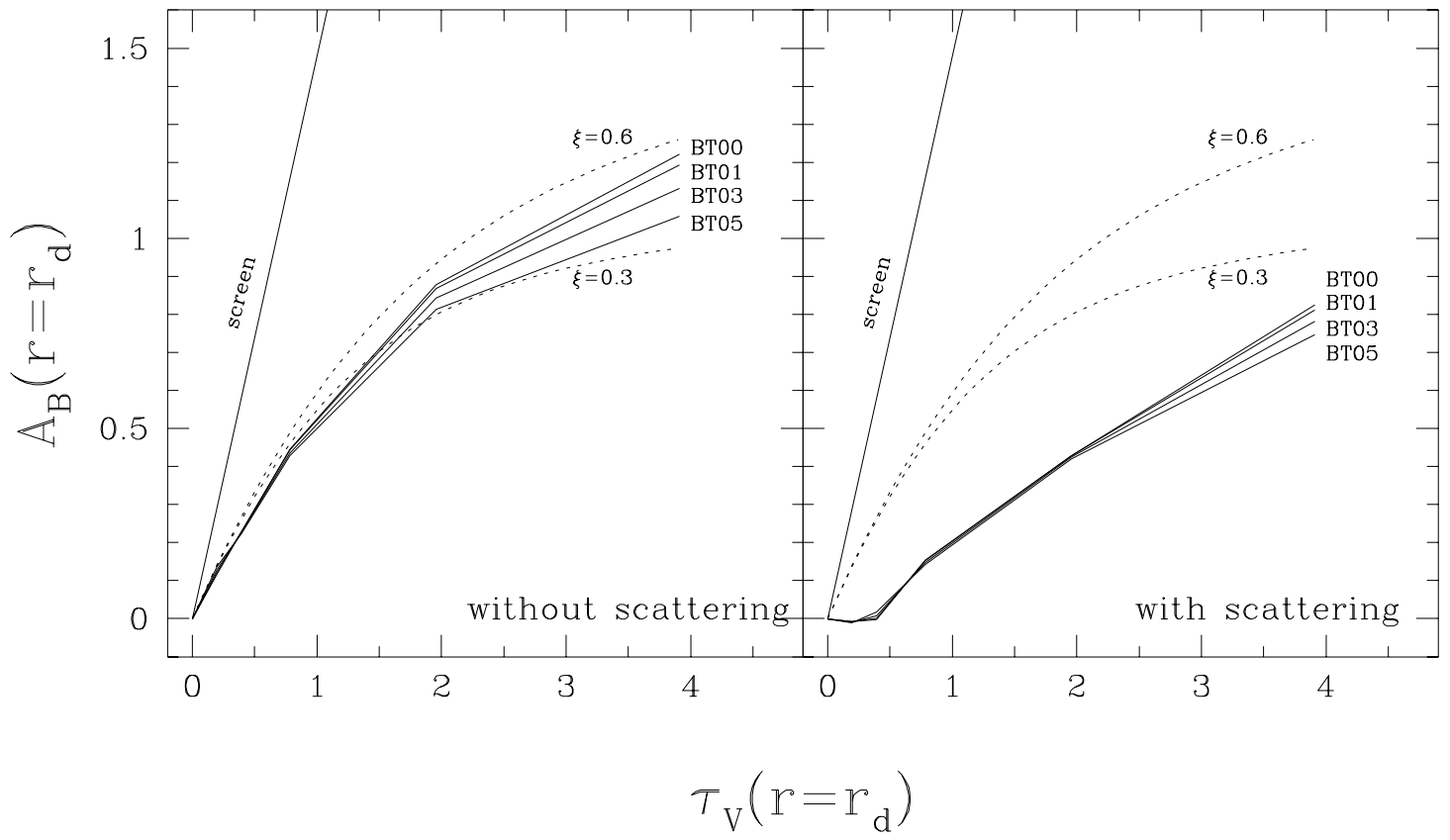
Fig. 13.— Scattering geometry in polar representation.



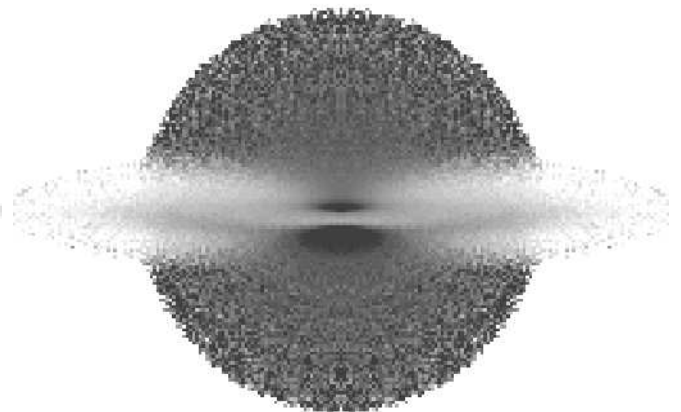
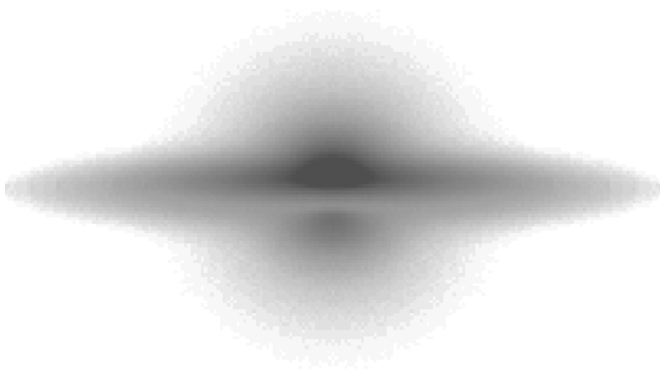
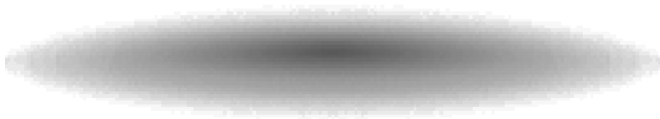
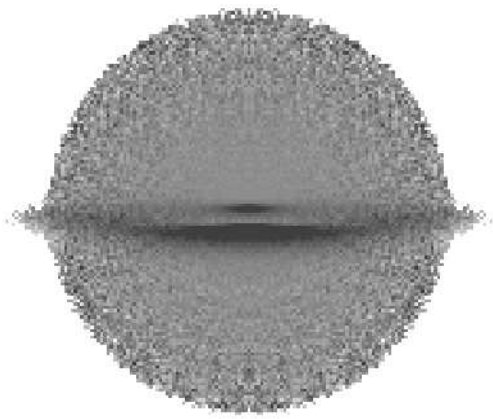
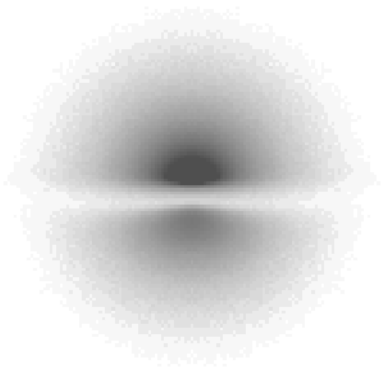


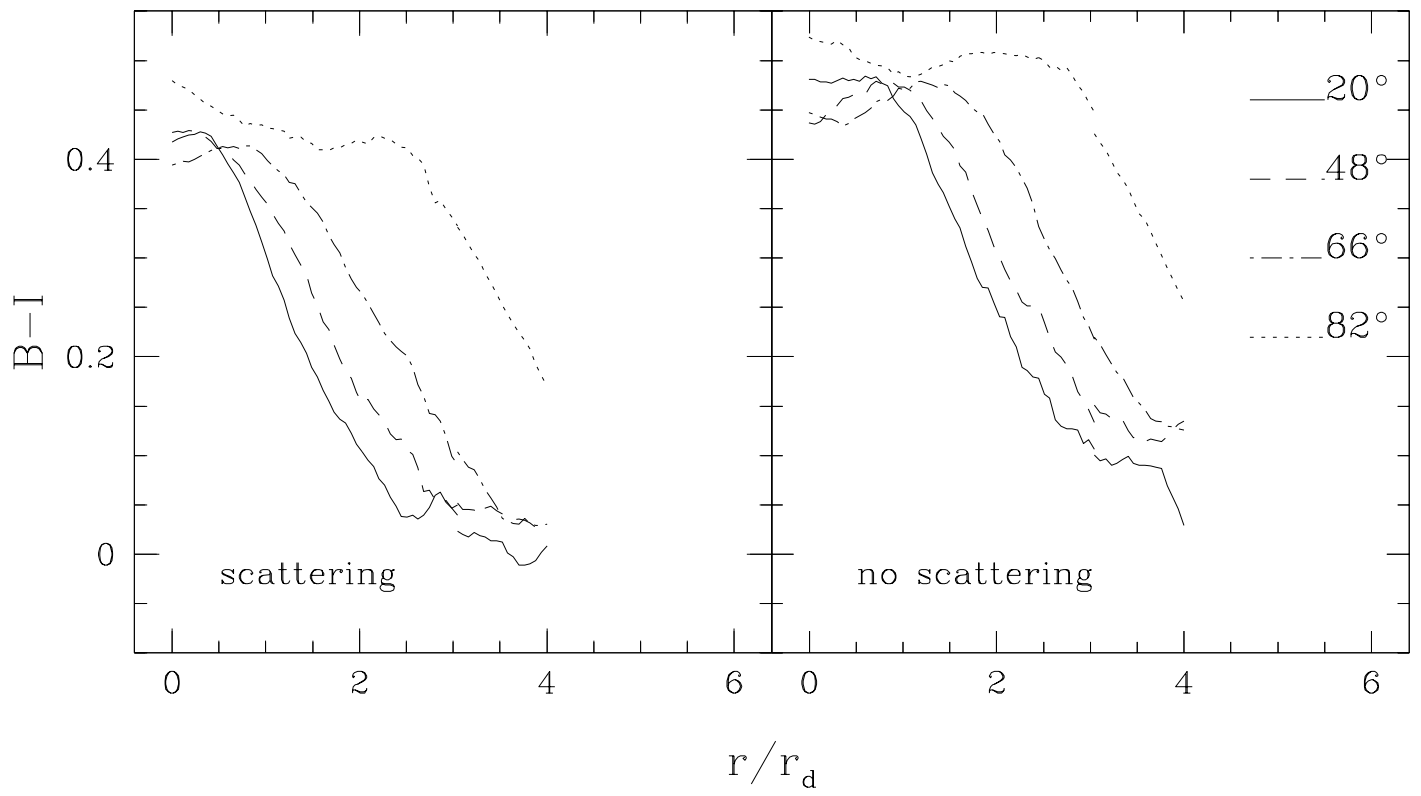




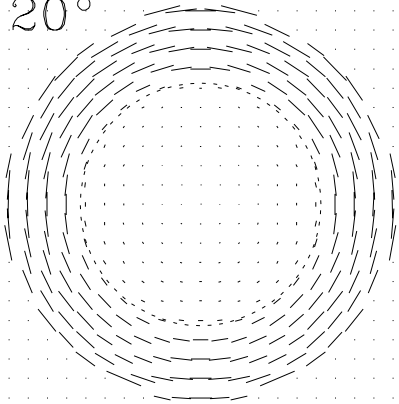




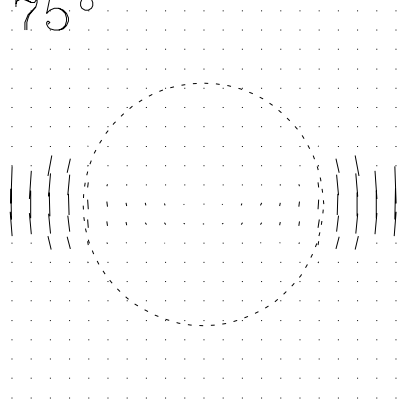




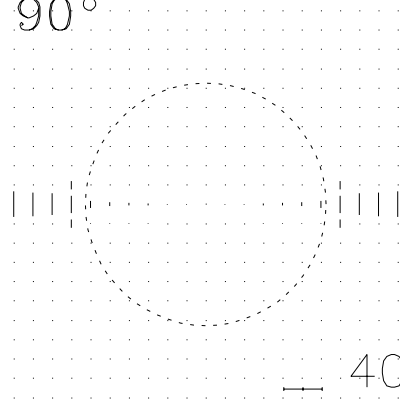
20°



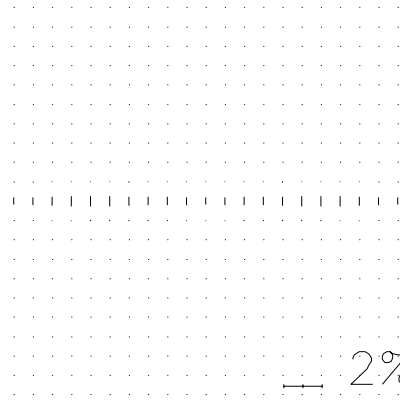
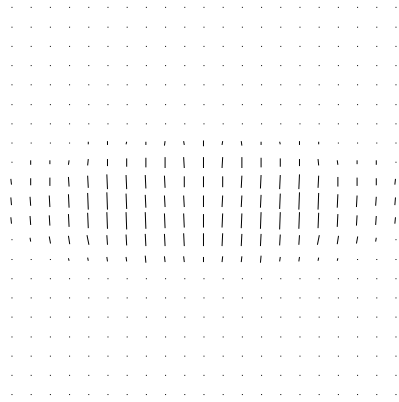
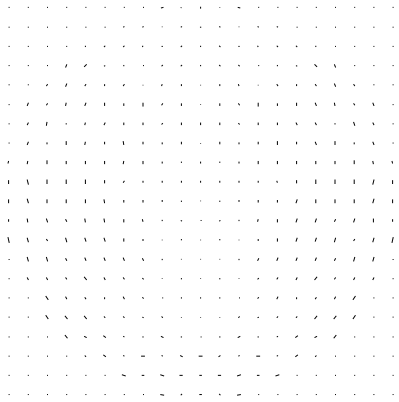
75°



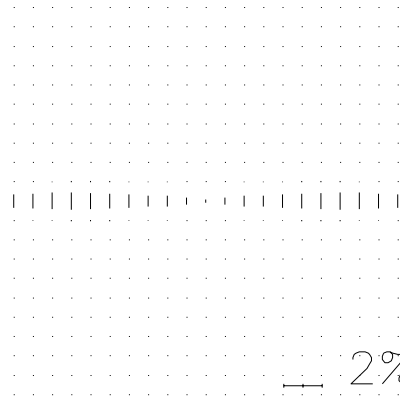
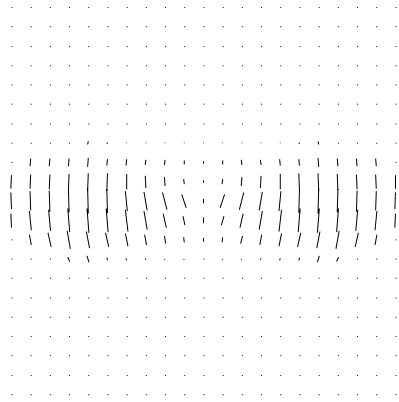
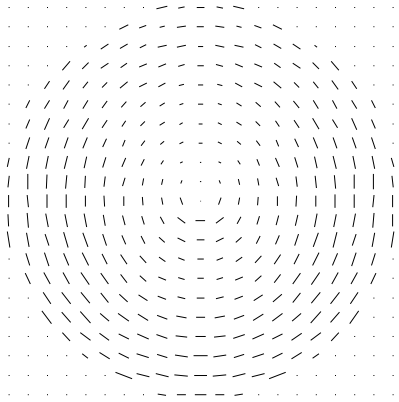
90°



— 40%



— 2%



— 2%

BT05 major axis

